Effect of binder content in Cu-In-Se precursor ink on the physical and electrical properties of printed $CuInSe_2$ solar cells

THE JOURNAL OF PHYSICAL CHEMISTRY C

Anatolian University Libraries Consortium a·n·k·o·s

Subscriber access provided by ONDOKUZ MAYIS UNIVERSITESI

Article

Effect of Binder Content in Cu-In-Se Precursor Ink on the Physical and Electrical Properties of Printed CuInSe Solar Cells

Marie Buffiere, Armin Esmaeil Zaghi, Nick Lenaers, Maria Batuk, Samira Khelifi, Jeroen Drijkoningen, Jonathan Hamon, Andre Stesmans, Jacek Kepa, Valeri V Afanas'ev, Joke Hadermann, Jan D'Haen, Jean V. Manca, Jozef Vleugels, Marc Meuris, and Jeff Poortmans

J. Phys. Chem. C, **Just Accepted Manuscript** • DOI: 10.1021/jp507209h • Publication Date (Web): 06 Nov 2014

Effect of Binder Content in Cu-In-Se Precursor Ink on the Physical and Electrical Properties of Printed $CuInSe_2$ Solar Cells

M. Buffière[1,2,9*], A.E. Zaghi[2,3,9], N. Lenaers[2,3,9], M. Batuk[4,9], S. Khelifi[5,9], J. Drijkoningen[6,7,9], J. Hamon[10], A. Stesmans[8], J. Kepa[8], V.V. Afanas'ev[8], J. Hadermann[4], J. D'Haen[6,7], J. Manca[6,7], J. Vleugels[3], M. Meuris[6,7], J. Poortmans[1,2,7]

[1] Department of Electrical Engineering (ESAT), KU Leuven, Kasteelpark Arenberg 10, 3001 Heverlee, Belgium

[2] imec- partner in Solliance, Kapeldreef 75, 3001 Leuven, Belgium

[3] Department of Materials Engineering (MTM), KU Leuven, Kasteelpark Arenberg 44, 3001 Heverlee, Belgium

[4] Electron Microscopy for Materials Science (EMAT), University of Antwerp, Groenenborgerlaan 171, 2020 Antwerp, Belgium

[5] Electronics and Information Systems department (ELIS), University of Gent, Sint-Pietersnieuwstraat 41, 9000 Gent, Belgium

[6] imec division IMOMEC - partner in Solliance, Wetenschapspark 1, 3590 Diepenbeek, Belgium

[7] Institute for Material Research (IMO) Hasselt University, Wetenschapspark 1, 3590 Diepenbeek, Belgium

[8] Department of Physics and Astronomy (FYS), KU Leuven, Celestijnenlaan 200D, 3001 Leuven, Belgium

[9] SIM vzw, Technologiepark 935, 9052 Zwijnaarde, Belgium

[10] Institut des Matériaux Jean Rouxel (IMN)-UMR 6502, Université de Nantes, CNRS, 2 rue de la Houssinière, BP 32229, 44322 Nantes Cedex 3, France

*Corresponding author: buffiere@imec.be; Tel: +32 16 28 12 05

Abstract

Printed chalcopyrite thin films have attracted considerable attention in recent years due to their potential in the high-throughput production of photovoltaic devices. To improve the homogeneity of printed $CuInSe_2$ (CISe) layers, chemical additives such as binder can be added to the precursor ink. In this contribution, we investigate the influence of the dicyandiamide (DCDA) content, used as a binder in the precursor ink, on the physical and electrical properties of printed CISe solar cells. It is shown that the use of the binder leads to a dense absorber, composed of large CISe grains close to the surface while the bulk of the layer consists of CISe crystallites embedded in a Cu_xS particle based matrix, resulting from the limited sintering of the precursor in this region. The expected additional carbon contamination of the CISe layer due to the addition of the binder appears to be limited and the optical properties of the CISe layer are similar to the reference sample without additive. The electrical characterization of the corresponding CISe/CdS solar cells shows a degradation of the efficiency of the devices, due to a modification in the predominant recombination mechanisms and a limitation of the space charge region width when using the binder; both effects could be explained by the inhomogeneity of the bulk of the CISe absorber and high defect density at the CISe/Cu_xS-based matrix interface.

Keywords: Photovoltaic; chalcopyrite; printing; characterization; additive.

I. INTRODUCTION

$Cu(In,Ga)Se_2$ (CIGSe) solar cells have reached the highest conversion efficiencies amongst all thin film technologies of up to 20 % at the laboratory scale.[1-3] Co-evaporation[1] and sputtering followed by selenisation[2] are well-established methods for the synthesis of the absorber in high efficiency devices. However, both techniques require expensive vacuum equipment with limited throughput. Therein, non-vacuum techniques for the production of CIGSe solar cells offer several advantages, such as low investment cost, higher production rates, large area uniformity and considerable improvement of material utilization. According to Hibberd *et al.*,[4] non-vacuum approaches for CIGSe deposition can be approximately classified into three different categories: (1) Electro-, electroless and chemical bath deposition where (electro)chemical reactions in a solution lead to the coating of an immersed substrate;[5-7] (2) Particulate-based processes that use solid particles dispersed in a solvent to form an ink, which can be coated onto a substrate;[8-11] (3) Processes that coat molecular precursor solutions onto a substrate by mechanical means such as spraying or spin coating.[12-16] The highest performance for CIGSe solar cells with an absorber made using a non-vacuum technique was obtained by Nanosolar using a nanoparticle ink-based device, claiming certified total-area efficiency of 17.1 %.[17] Todorov *et al.* have recently demonstrated the potential of the solution ink-based technique by yielding up to 15.2 % efficiency solar cells.[18] Various promising results from different groups using particle or molecular based inks have been reported.[19, 20]

To improve the homogeneity of printed absorber layers (categories 2&3), chemical additives can be added to the precursor ink. In order to get crack-free precursor thin films, organic binders are in general used to bind the particles forming the precursor once the solvent evaporates. However, using additives might also have drawbacks on the solar cell performances when resulting in the

contamination of the absorber. Carbon is one of the most problematic contaminants, since it can form stable clusters during the annealing step[21] and is therefore very difficult to remove from the absorber layer. In the case of solution ink-based precursor, the use of C-based solvent/binder leads to a residual carbon layer between back contact and absorber.[22] Although the related devices still reach reasonable efficiencies and the C-rich bottom layer does not seem to hinder the electrical properties of the solar cells,[23] the impact of the C-related defects in the CISe material as well as the influence of chemical additives in the precursor ink on the properties of the absorber remains unclear. In this contribution, we report on the influence of the dicyandiamide (DCDA) concentration, used as a C-based binder in the precursor ink, on the properties of printed $CuInSe_2$ (CISe) solar cells. A detailed analysis, consisting of both physical and electrical measurements, was carried out on the devices.

II. EXPERIMENTAL

Synthesis of printed CISe solar cells

The precursor ink was prepared using mechanically alloyed Cu-In-Se nanopowder. Elemental high purity powders of Cu, In and Se were weighted to give a molar ratio of Cu:In:Se= 0.85:1:0.5 as selected from a previous study[24] but the ink also contains sulfur impurities (about 3 at.%). The Cu-In-Se precursor powder was synthesized from the elemental powders by dry planetary ball-milling, i.e. mechanical alloying, in yttrium stabilized zirconia (YSZ) ceramic milling jars, using first 10 mm YSZ ceramic milling balls in inert atmosphere, followed by a second milling step in wet medium using 3 mm YSZ milling balls in order to obtain a nanopowder. The Cu-In-Se nanopowder is then dispersed in an alcohol (1,5-Pentanediol). More details about the preparation of the precursor ink can be found elsewhere.[25] In order to study the influence of the binder content in the absorber layer on the properties of the resulting solar cells, DCDA ($C_2H_4N_4$) was dissolved in dimethyl

sulfoxide (DMSO) and added to the ink in different concentrations (i.e. (a) 0 wt.%, (b) 10 wt.%, (c) 20 wt.% with respect to the Cu-In-Se precursor mass in solution). The resulting inks were printed using the Doctor Blade technique on molybdenum coated soda lime glass (SLG/Mo) and dried on a 100 ˚C hot plate in nitrogen atmosphere for 1 hour. The morphology of the precursor layer after the drying step is visible in part A of the supporting information. Then, they were annealed in selenium vapor using a two-step process (250 ^{o}C, 10 min; 500 ^{o}C, 20 min) to obtain polycrystalline CISe thin films. The preparation process of this series of samples is summarized in Figure 1. Reference CISe layer grown by co-evaporation using a Cu-PRO process[23] were also synthesized. For completing the thin film solar cell structure, a standard procedure for CIGSe based solar cells was used, consisting of a KCN etch to remove the Cu_xSe secondary phases and the excess of selenium, a chemical bath deposition of a thin n-type CdS buffer layer and RF-sputtering of 60 nm of intrinsic ZnO followed by 350 nm of highly Al-doped ZnO. Finally, a 50 nm Ni - 1 µm Al finger grid pattern was evaporated through a shadow mask for top contact formation. Lateral isolation of the cells was performed by needle scribing. In this way, solar cell devices with sizes ranging from 0.5 cm^2 to 1 cm^2 were fabricated on the 2.5x5 cm^2 samples.

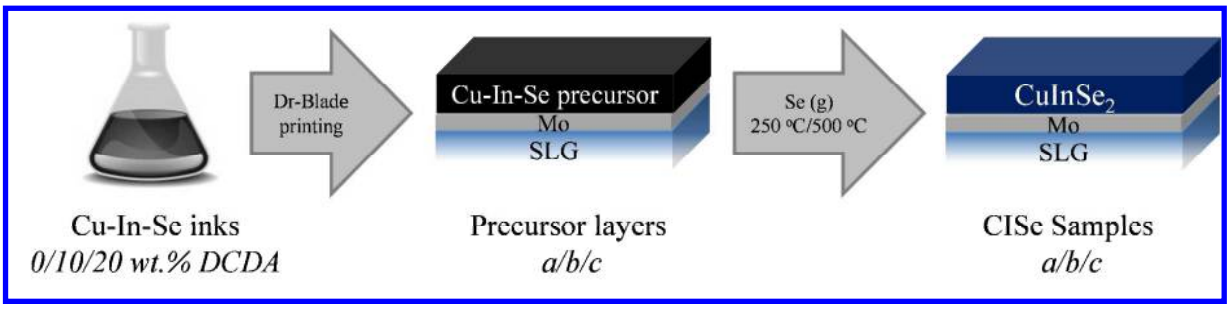

Figure 1. Scheme of the process used for the preparation of the samples studied in this work.

Physical characterization

The morphology and chemical composition of the CISe thin films were evaluated by scanning electron microscopy (SEM, XL-30-FEG, Philips), equipped with an energy dispersive X-ray analysis system (EDX). The microstructure of the solar cells was investigated by transmission electron microscopy (TEM, FEI Tecnai G2 microscope operated at 200 kV). Cross-section specimens for TEM study were prepared using focused ion beam milling (FIB, Helios NanoLab 650 machine). In order to preserve the surface layer of the sample, a Pt/carbon protective layer was deposited prior to the sample preparation. High angle annular dark field scanning transmission electron microscopy (HAADF-STEM) images and EDX elemental maps were recorded using a FEI Titan 80-300 "cubed" microscope equipped with a Super-X detector and operated at 200 kV. EDX maps were generated from the intensity of the Cu-K, In-L, Se-K, Cd-L, S-K, Zn-K, O-K, C-K, and Mo-K lines. X-ray photoemission spectroscopy (XPS, AXIS Nova, Kratos) was performed on the printed CISe layer using a monochromatic Al K_α X-ray source (1486.6 eV) running at 150 W. The base pressure in the analysis chamber was 10^{-8} mbar and the analysed area was 700×300 μm^2. The argon ion bombardment in the XPS system was used to *in-situ* etch the CISe thin films surface in order to have access to the bulk of the absorber. The etchings were performed at 4 keV for different time duration. The argon gas purity was 99.999 %. The density of C-related defects was characterized by electron spin resonance (ESR) spectroscopy. ESR measurements were done on samples printed and annealed on quartz substrates and subsequently removed from the substrate to obtain the samples in the form of powder. After weighting, the samples were mounted in the cavity of a K-band (20.5 GHz) ESR spectrometer. Classical absorption-derivative ESR spectra were measured at liquid helium temperature (4.3-5 K) in the slow adiabatic passage mode. Calibration of the signal intensity and g-value has been done relative to a co-mounted Si:P marker sample (g=1.99869 at 4.3 K). The optical properties of the CISe thin films printed on quartz substrates using different binder concentrations were studied by optical transmission (T) measurements in the spectral range 1.8-0.4 μm using a 250 W tungsten lamp as the light source and an InGaAs photodiode as detector.

Electrical characterization

Conductive atom-probe force measurements (C-AFM, MultiMode8, Bruker) and Kelvin probe force measurements (KPFM, MultiMode8, Bruker) were recorded in an inert nitrogen atmosphere on the surface of the different SLG/Mo/CISe samples. The delta deflection set point during C-AFM imaging was kept below 0.6V to exclude the possibility of tip and sample degradation. The drive amplitude during KPFM was kept at 3000 mV while using a lift scan height of 20 nm. For both C-AFM and KPFM Pt/Ir tips were employed. The force constant was 0.4 N/m for C-AFM and 4 N/m for KPFM. The Canny-edge multi-stage algorithm was used to detect edges in images and defines edges as zero-crossing of second derivatives in the direction of greatest first derivative. The processed solar cells were analyzed using current-voltage (I-V, 2600 Sourcemeter, Keithley) measurements performed under a solar simulator system (Model 6143, Oriel) using an AM1.5D spectrum with an illumination density of 1000 W/m^2. Capacitance-voltage (C-V, analyzer: HP 4192A LF) measurements were performed using a impedance analyzer (5 Hz-13 MHz). Temperature dependent measurements were performed using a cold finger cryostat mounted on a nitrogen source. For I-V-T measurements under different illumination intensities, a solar simulator was used together with neutral filters to get different illumination levels from about 1 to 1000 W/m^2.

III. RESULTS AND DISCUSSION

A. *Analysis of the CISe absorber layers*

Figure 2(a-c) shows the typical top view and cross-section SEM images of CISe thin films synthesized from a precursor ink without DCDA and with an intermediate (i.e. 10 wt.%) or a high content (i.e. 20 wt.%) of this binder. The cross-section SEM images show that the three samples exhibit a similar bilayer morphology, which is composed of a poorly sintered "bottom" layer of about 1 µm thick with an apparent grain size in the nanometer range, and a thinner "top" layer of large CISe grains. In the case of the samples synthesized with binder, this bilayer morphology is more pronounced, with larger grains on the top (up to 1 µm as observed on the top view SEM images) and a denser bottom layer, than for the CISe layer printed without additive. Therefore, it seems that the use of a binder leads to the improvement of the sintering of the Cu:In:Se nanopowder into large CISe crystallites on the top area, i.e., close to the heater and to the selenium supply during the annealing step, and to the densification of the deeper absorber region, which prevents the formation of cracks. No major morphological change is observed when increasing the binder content from 10 wt.% to 20 wt.% in the precursor ink.

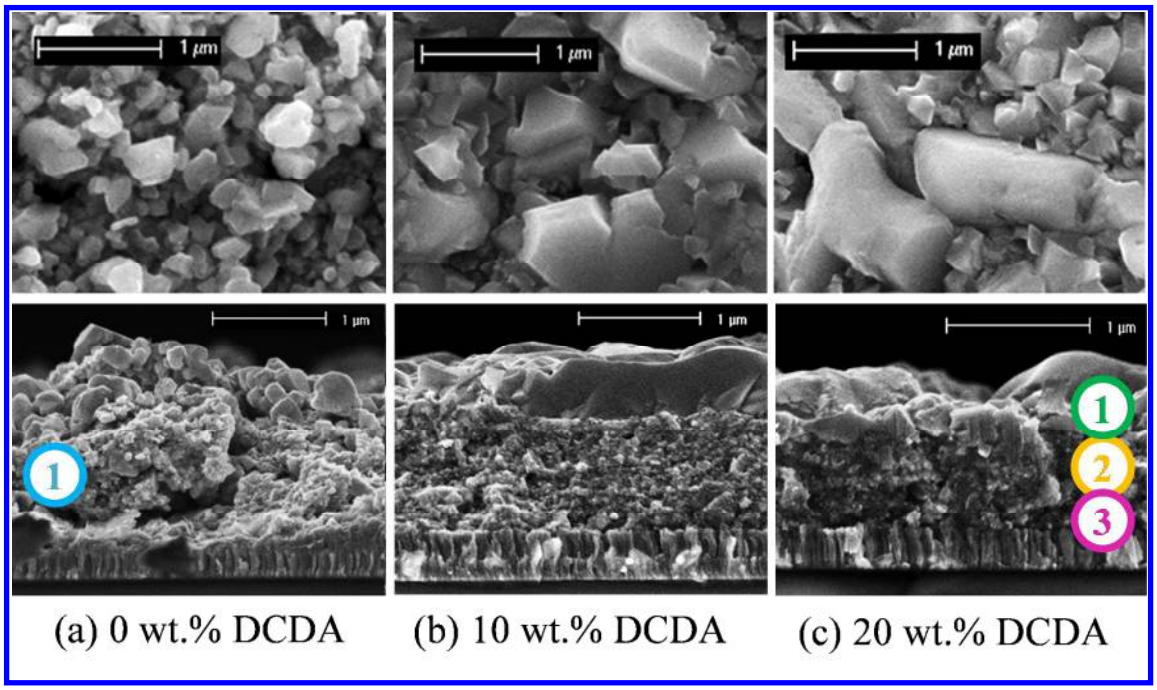

Figure 2. Top view (upper row) and cross-section (lower row) SEM micrographs of printed CISe absorbers synthesized using (a) 0 wt.%, (b) 10 wt.% or (c) 20 wt.% of binder. The locations (1-3) indicates the in-depth positions of the XPS analysis (see figure 3).

A poorly sintered bottom layer is often reported in the case of printed chalcogenide absorbers.[26,27] In order to check the chemical composition at this specific location, XPS analyses were performed on the printed absorbers without and with 20 wt.% of DCDA. Ion gun etching was used to analyze different in-depth positions in the CISe layers. These positions are indicated on the X-SEM images of Fig. 2. The full spectrum analysis (not shown here) confirms the presence of Cu, In, Se as well as a low concentration of C and O in both layers for the different locations. Figure 3 shows the spectra of both samples corresponding to the C 1*s* peak position, recorded using the same conditions. These spectra must be considered with caution, since the position of the C 1s peak and the Se $L_3M_{23}M_{45}$ Auger signal are at the same location when using an Al K_α X-ray source. The intensity and the position (284.6 eV) of the visible peak are similar for both samples, i.e., similar C contents if this peak correspond to the C 1*s* signal, or limited C content if this peak corresponds to the Se $L_3M_{23}M_{45}$ signal, which would confirm that the additional contamination due to the DCDA additive is limited, and that the bottom CISe layer does not contain a significant amount of organic matter. When increasing the etching duration, a second peak located at 283.6 eV becomes visible, which could be due to the presence of metallic carbide compounds (such as Mo_2C, In_4C_3, etc.) formed during the erosion of the sample.

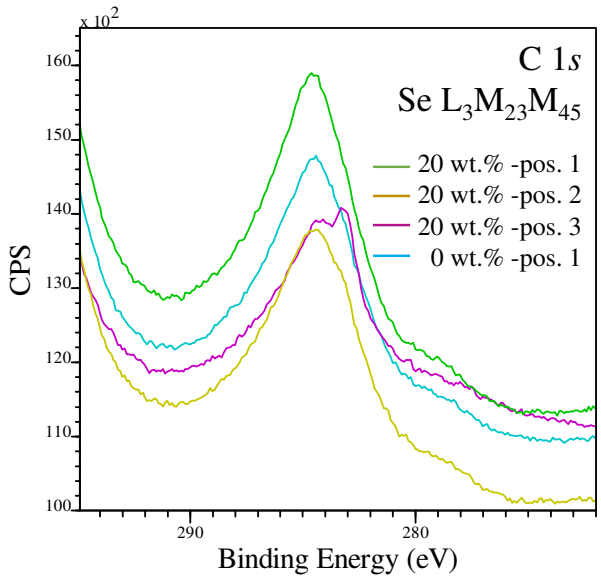

Figure 3. XPS spectra of the samples without and with 20 wt.% of DCDA in the region of the C 1*s* XPS peak. The in-depth position mentioned correspond to the locations indicated in figure 2.

Table 1 shows the Cu/In ratio of similar layers without binder and with 10 wt.% or 20 wt.% binder contents deposited on a quartz substrate and of a reference CISe layer deposited by co-evaporation, as measured by EDX. All of them are Cu-poor (i.e. [Cu]/[In] < 1) with a Cu content slightly higher than the precursor ink, indicating some losses in In during the processing of the layer. The CISe layers with DCDA have a Cu-ratio which is slightly higher than the sample without binder, which could be due to the inhomogeneous distribution of Cu in the non-sintered bottom layer. According to the ESR measurements performed on these samples, all the printed layers after annealing contain about 1 ppm of defects related to carbon dangling bond centers at the characteristic g-factor value of ≈2.0035 (although the nature of these defects seems to be different between the CISe layers with or without DCDA- see the supporting information, part B). By contrast, the co-evaporated CISe reference does not show any detectable carbon traces. The residual carbon impurities could come from the solvent used for the preparation of the precursor ink, while the use of

the binder does not seem to increase the density of the C-related defects in the printed absorber layer as could be expected (although the total C content could still be higher). However, only the un-annealed and co-evaporated CISe layers show Cu^{2+} signals in ESR measurements, indicating the presence of not fully bonded Cu atoms. More details about the ESR spectra can be found in the part B of the supporting information.

Table 1. Chemical composition as measured by EDX and dangling bond densities related to C and Cu as determined from the ESR spectra of the printed CISe absorbers with different binder content values as compared to the co-evaporated CISe reference sample.

Sample	Cu/In ratio	C density (g^{-1})	Cu^{2+} density (g^{-1})
0 wt.% DCDA	0.87	3.0(±0.4)E+17	≤1.0E+13
10 wt.% DCDA	0.98	2.4(±0.4)E+17	≤1.0E+13
20 wt.% DCDA	0.94	2.5(±0.3)E+17	≤1.0E+13
$CuInSe_2$ ref.	0.90	≤1.0E+13	7.3(±0.9)E+17

As the morphological change between the printed CISe layers with and without binder could induce a modification of the optical properties of the absorber, spectral transmittance (T) curves of the samples deposited on quartz were recorded and compared to the CISe reference (Fig. 4.a). A first estimate of the product of the absorption coefficient and the CISe layer thickness (αd) was calculated from the T spectral curves using the Lambert-Beer law to enable determination of the absorption edge energy (cf. Fig. 4(b)). Since the CISe layers with binder are denser than the printed layers without additive, the latter is slightly thicker for the same quantity of printed material which may

explain a somewhat lower transmittance level. For all samples, similar band gap values were found (0.99 eV), which is in good agreement with the theoretical band gap of CISe.

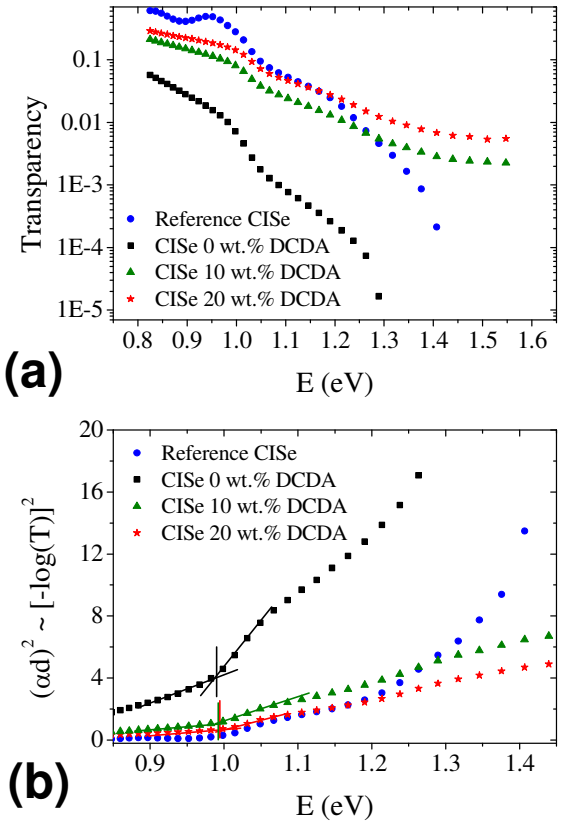

Figure 4. Optical (a) transparency (a) and relative absorption (b) spectra of the printed CISe samples without or with 10 wt.% or 20 wt.% of DCDA as compared to the co-evaporated CISe reference sample.

The electrical properties of the printed layers were then compared using AFM techniques. Figure 5 shows AFM and C-AFM mapping at a sample bias voltage of 2.5 V of the printed CISe thin films without (a, b), with 10 wt.% (c, d) or 20 wt.% (e, f) of DCDA binder. The AFM measurements confirmed the reduced average roughness of the CISe layer when using the binder. The C-AFM data shows that, when adding binder, the current at fixed bias increases significantly. This increase in current can be explained by the increased density of the film, since an increase in density should result in more conducting paths between the tip and Mo back contact. The larger grain size for the sample with binder leads to the decrease of the density of grain boundaries. The analysis of the grain boundaries by canny edge detection on using AFM topography and KPFM signal shows that grain boundaries visible in topography might not always be electronically active (see the supporting information, part C).

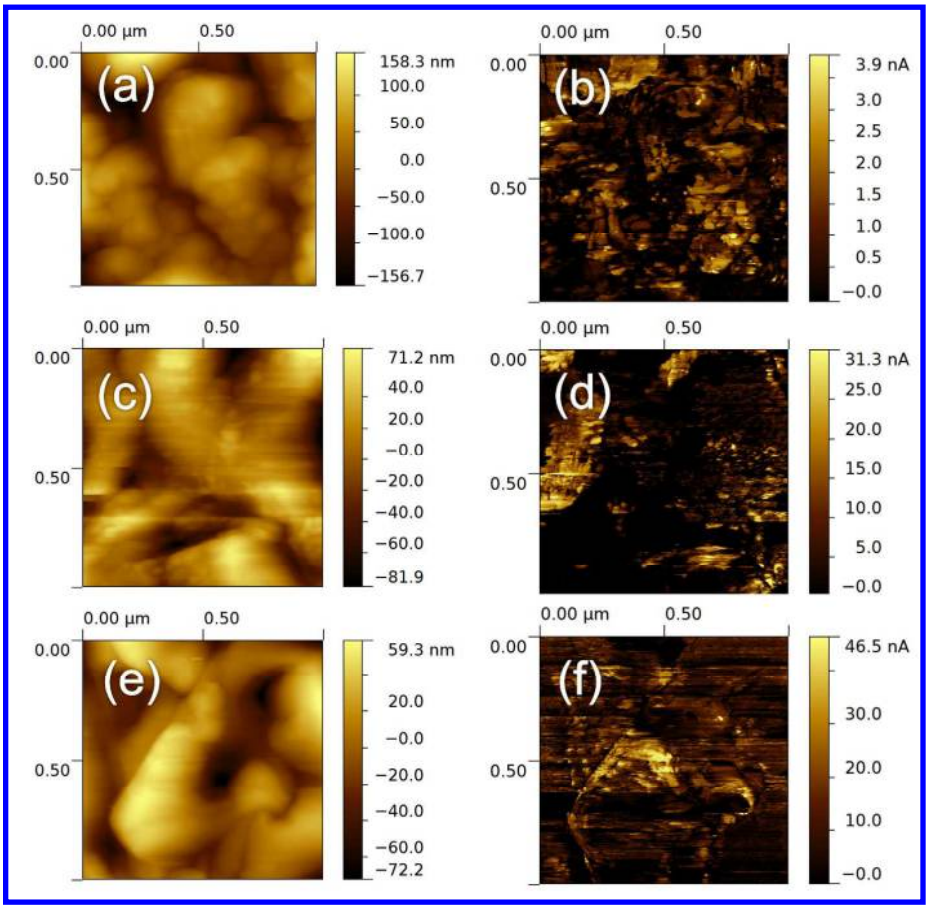

Figure 5. AFM (a, c, e) and C-AFM (b, d, f) mapping of the printed CISe thin films without (a, b), with 10 wt.% (c, d) or 20 wt.% (e, f) of DCDA binder.

B. Characterization of the corresponding solar cells

The samples (a), (b) and (c) were used as absorber layers in a complete SLG/Mo/CISe/CdS/ZnO/AZO solar cell structure in order to evaluate their electrical performance. The main electrical parameters extracted from the I-V curves of the 6 best solar cells per sample are presented in Figure 6(a). The best solar cell (J_{sc} = 30 mA/cm^2, V_{oc} = 371 mV, FF = 44 %, η = 4.8 %) and the best average efficiency were obtained for the sample without binder. When increasing the DCDA binder content into the precursor ink, the resulting solar cells show an overall decrease of the electrical parameters (i.e. J_{sc}, V_{oc}, FF, and therefore, efficiency), which could appear in contradiction with the improvement of the absorber morphology. The shunt and series resistance (R_{sh} and R_s respectively) of the devices were extracted from the 2-diode model using $n_1 = 1$, $n_2 = 2$ (Fig. 6(b)). One can see that this overall decrease of the electrical parameters, when increasing the DCDA binder content into the precursor ink, is accompanied by a decrease in R_{sh} and an increase in Rs. Although the dispersion of the R_{sh} values is improved when using the additive - likely because of the decrease of the crack density - this parameter systematically dropped below 100 Ω.cm^2 for the samples using the DCDA binder while Rs increased to an average value of more 10 Ω.cm^2.

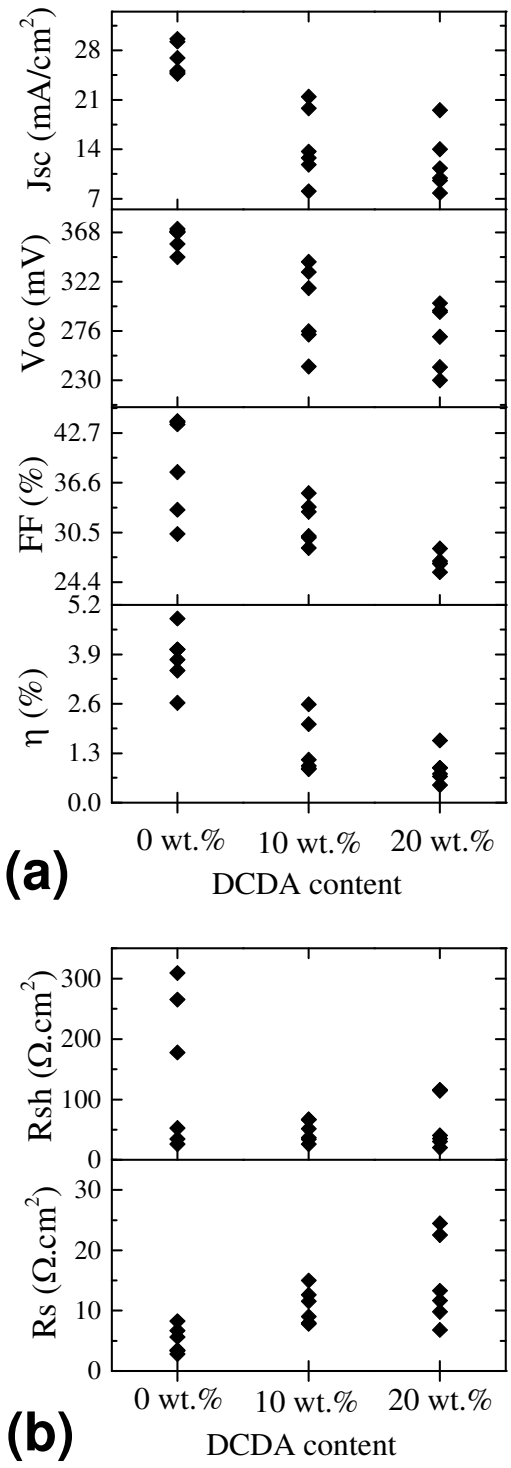

Figure 6. Electrical parameters ((a) V_{oc}, J_{sc}, FF, η and (b) R_s, R_{sh}) of the six best printed CISe solar cells using inks containing no binder, 10 wt.% or 20 wt.% of DCDA.

C-V measurements were performed on the best solar cells and compared to a co-evaporated CISe reference solar cell having an efficiency of 12 %. Figure 7 shows that the doping level of the reference sample is about 10^{16} cm^{-3}, which is consistent with literature.[28] The analysis of the printed samples shows that the best device (i.e. without binder) has the larger apparent space charge region (SCR), about 0.5 μm. The doping density is similar to that of the reference sample. Increasing the binder content seems rather to reduce the SCR width in the absorber (to about 0.2 μm) than to change the doping level in the absorber, which could eventually explain the limited J_{sc} values obtained on the samples with binder. This would confirm that the quality of the top CISe layer is similar for all printed samples, but the electrically active region of the absorber seems to be limited to the upper region of the absorber where the additive-based layers are concerned. I-V-T measured from 200 K to 320 K every 20 K under different light intensities were also performed in order to investigate the possible recombination mechanisms in the different devices. Figure 8 shows the V_{oc} of the cells as a function of temperature. For the sample without additive (Fig. 8(a)), the behavior is linear down to 200 K, and the extrapolation of the linear trend to zero K yields to a value (around 1.0 eV) close the band gap value (0.99 eV as extracted from the transmittance measurements). For the samples with 10 wt.% and 20 wt.% DCDA (Fig.8(b) and Fig.8(c) respectively), the extracted values (0.82 and 0.77 eV respectively) are clearly below the band gap values; in this case, the activation energy of the main recombination process seems to be limited by a reduced band gap somewhere at the interfaces, which could explain the V_{oc} limitations of the devices. The consistency between the activation energy and the band gap value in the case of the CISe solar cell made without binder indicates dominant recombination mechanisms located in the bulk or the SCR of the absorber.

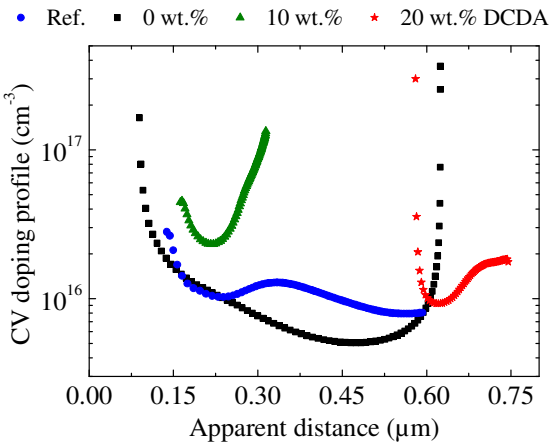

Figure 7. C-V doping profiles for the solar cells using printed CISe absorbers without binder, with 10 wt.% or 20 wt.% of binder and a co-evaporated CISe absorber as reference.

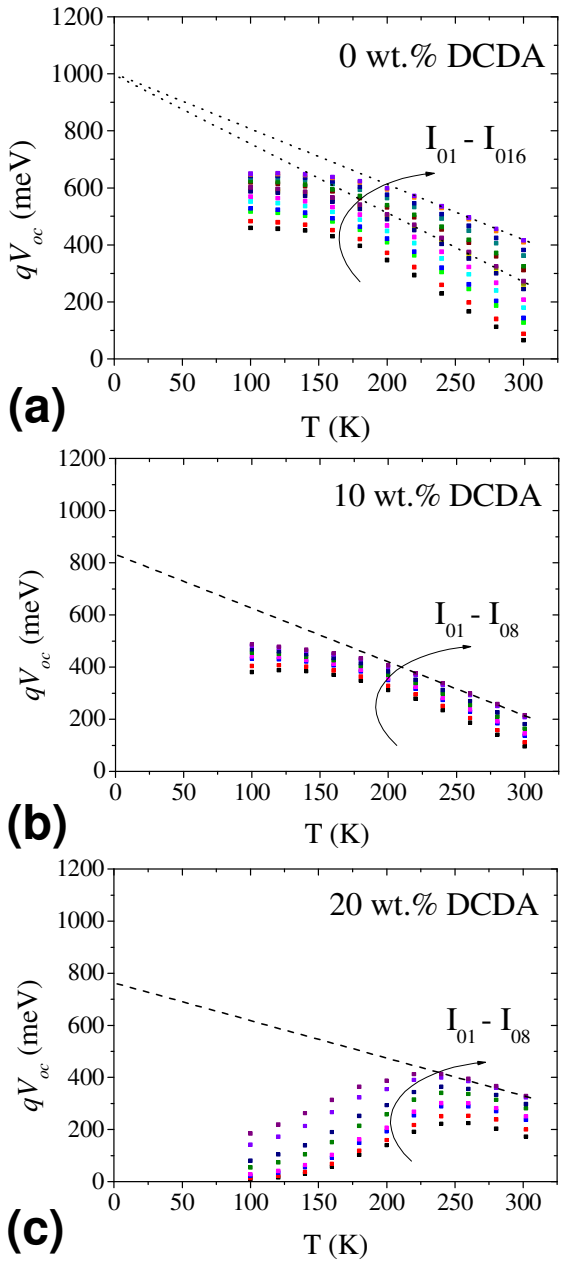

Figure 8. V_{oc} as function of temperature deduced from I-V-T measurements using different light intensities (from 0.1 sun to 1 sun) for the CISe devices (a) without and with (b) 10 wt.% or (c) 20 wt.% of binder.

In order to better understand the impact of the DCDA binder content on the electrical behavior of printed CISe solar cells, TEM analyses were performed on the cross-section of these samples. Overview HAADF-STEM images of the films are shown in Figure 9(a-c). The TEM analysis confirms the results obtained from the SEM study (Fig. 2) that increasing of the binder content from 0 wt.% to 20 wt.% leads to a decreased crack density through the CISe layer and increase of the bottom CISe layer density. Individual small CISe grains are seen in the sample without binder (Fig. 9.d); they are covered with an amorphous layer with a thickness of about 10 nm. In the sample with 20 wt.% of binder, such small grains appear to be highly agglomerated (Fig. 9.e); their surface is clear of any amorphous phases. Surprisingly, large CISe grains were also observed in the bottom layers of both samples. EDX maps for the samples without and with 20 wt.% of binder are shown in Figures 10 and 11, respectively, with (a) the HAADF image of the sample and (b-h) the EDX maps of Cu, In, Se, Cd, S, C and O respectively. According to the EDX maps in Figure 10, the thin amorphous layer covering the CISe grains (both large and small) is mainly CdS phase. In this sample, the CdS layer deposited by CBD on the CISe surface goes through the CISe grain boundaries and cracks to nicely cover the free surface of small grains of the non-dense bottom layer region. For the second sample, the CISe grains in the bottom part are surrounded by Cu_xS particles in the nanosize range, which likely originated from the milled precursor itself or from the complexation reaction between DMSO, DCDA and Cu from the precursor. In addition, the particles of Cu_xS phase are present among the small CISe crystal. Very small amounts of C and O are detected in both samples, with a little amount of organic matter segregated at the grain boundaries and in the bottom layer. However, one should keep in mind that the samples are easily contaminated under the electron beam (which leads to the increase of the C signal on the EDX maps) and therefore the carbon EDX maps should be treated with care. The thickness of the CdS layer on top of the CISe layer is increased in a row (from ~15 nm for the sample without binder to ~50 nm for the CISe layer with additive). Another

noticeable difference between the samples is the degradation of the Mo layer in the films with higher binder content.

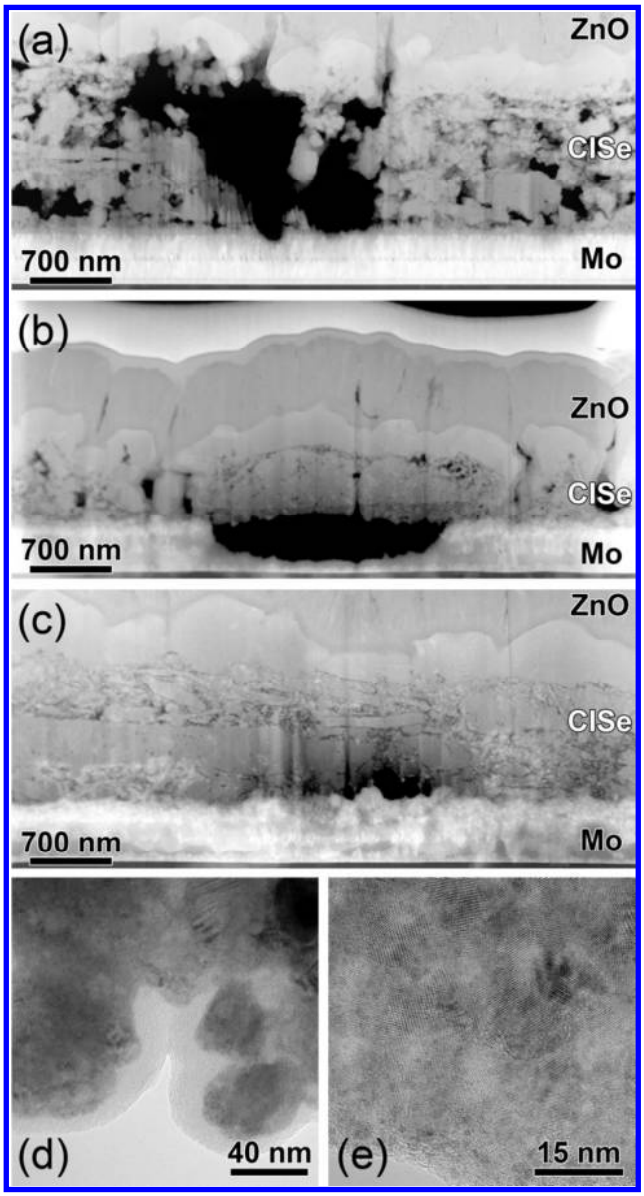

Figure 9. Cross-section STEM images of the best solar cells using CISe printed absorbers from an ink containing (a) no binder, (b) 10 wt.% or (c) 20 wt.% of DCDA. The TEM analysis of the free surface of the bottom CISe grains is shown in figure (d) (samples without binder) and (e) (sample with 20 wt.% of binder).

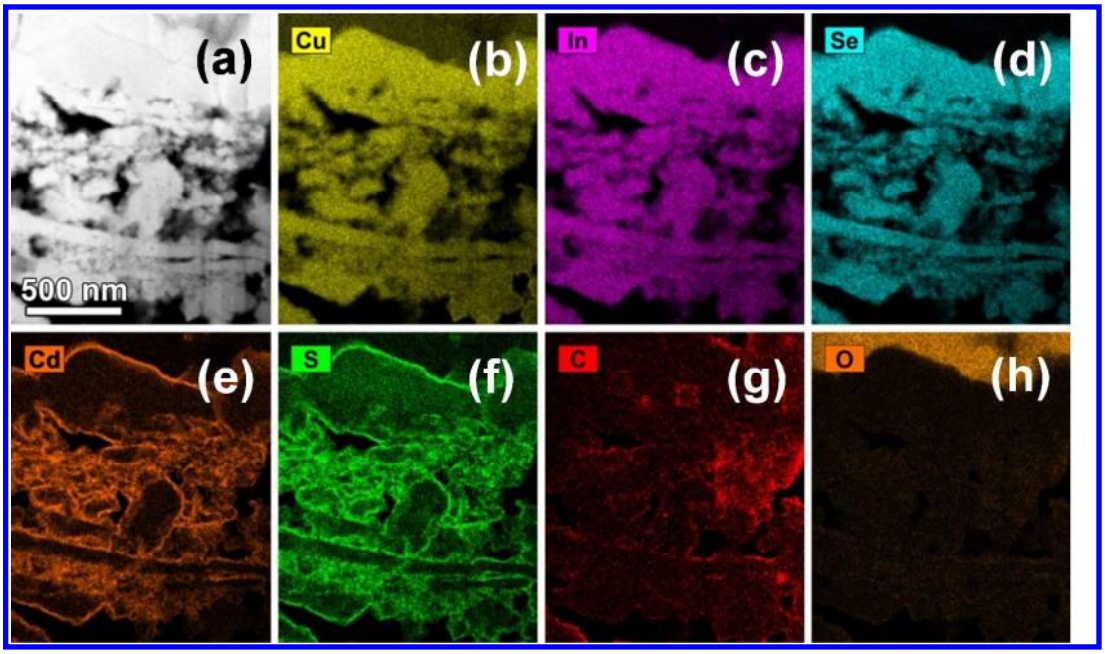

Figure 10. Cross-section HAADF-STEM image (a) and EDX maps of Cu (b), In (c), Se (d), Cd (e), S (f), C (g) and O (h) of the best printed CISe solar cell without binder.

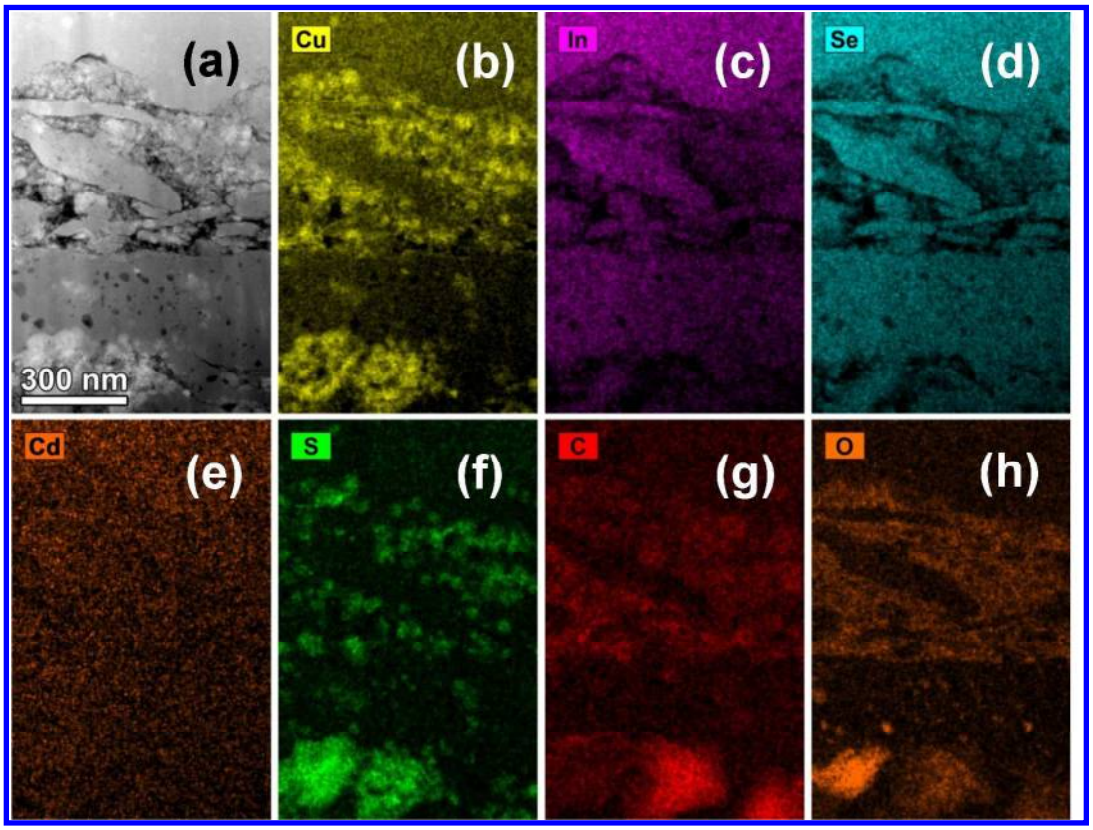

Figure 11. Cross-section HAADF-STEM image (a) and EDX maps of Cu (b), In (c), Se (d), Cd (e), S (f), C (g) and O (h) of the best printed CISe solar cell with 20 wt.% of binder.

The microstructure of the printed CISe absorber when using DCDA as a binder could be a suitable explanation of the electrical performances of the corresponding solar cells. Densifying the precursor layer to reduce the crack density also leads to two unexpected consequences : (1) the presence of a dense Cu_xS-rich matrix filling the voids between the CISe grains of the bottom part of the absorber; (2) and consequently, the non-covering of the bottom CISe grains by the CdS buffer layer (see Fig. 12). By improving the density of the bottom CISe layer, the sintering of the nanopowder precursor -containing among other Cu_xS particles[27]- is rather limited due to the limited diffusivity of Se into the dense precursor layer, while the binder improved the sintering of the CISe grain on the top surface. The non-sintered part of the precursor which forms the environment of the bottom CISe grains is assumed to have metallic electrical behavior, as Cu_xS phases are a p-type degenerated semi-conductor material. Since the grains embedded in this semi-metallic matrix are not covered by the CdS buffer layer, we can assume that the density of electrical defects at the surface of these CISe crystals is higher than for the top CISe grains, which would lead to high recombination rates of the carriers at the CISe/Cu_xS-based matrix interface. In this case, the p/n junction is limited to the front CISe/CdS/ZnO interface, and a limited amount of carriers generated in the CISe bottom grains can be gathered. This model is in good agreement with the limited space charge region and the dominant interface recombination mechanism observed in the samples with binder. For the top CISe grains, the semi-metallic matrix acts as a p-type electrode, allowing the photoelectron current to flow but also adding an additional series resistance which could come from the higher resistivity of this matrix compared to the Mo back contact, eventually due to carbon residue not detected by XPS. In the case of the sample without binder, the porous layer promotes a more efficient conversion of the precursor into CISe and/or allows the KCN solution to deeply remove any Cu_xS particles. The surface passivation by CdS of the bottom chalcopyrite crystals can lead to the modification of the predominant recombination mechanism and of the defect density in the SCR. Furthermore, the interconnection between the bottom and top CISe grains ensures the collect of the minority carriers

coming from the bottom part of the absorber. However, this type of structure results in low and inhomogeneous shunt resistance values, limiting the efficiency of such type of solar cells.

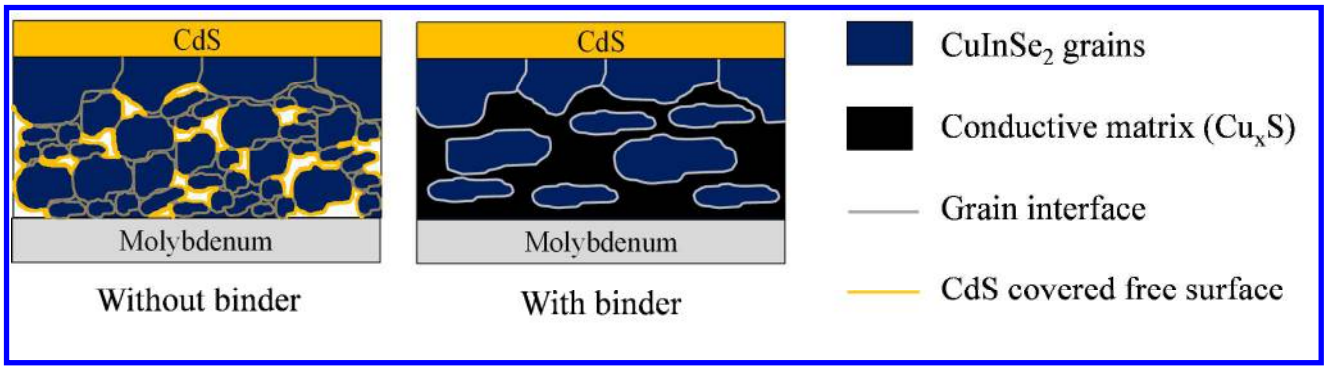

Figure 12. Model representing the morphology of CISe printed absorbers without and with binder.

IV. CONCLUSION

With the aim of improving the homogeneity of printed CISe absorber for photovoltaic applications, we investigated the influence of the dicyandiamide (DCDA) content, used as a binder in the precursor ink, on the physical and electrical properties of CISe solar cells. We have observed that the use of the binder leads to a dense absorber, which is composed of large CISe grains close to the surface while the bulk of the layer consists of large CISe crystallites embedded in a Cu_xS particle based matrix, resulting from the limited conversion and sintering of the precursor in this region. The expected additional carbon contamination of the CISe layer due to the addition of the binder appears to be limited and the optical properties of the CISe layer are similar to the reference sample without additive. The electrical characterization of the corresponding CISe/CdS solar cells show a degradation of the efficiency of the devices, due to a modification in the predominant recombination mechanisms and a limitation of the space charge region width when using the binder; both effects could be explained by the inhomogeneity of the bulk of the CISe absorber and high defect density at the CISe/Cu_xS-based matrix interface.

Acknowledgments

This work is supported by the 'Strategic Initiative Materials' in Flanders (SIM) and the Institute for Innovation through Science and Technology in Flanders (IWT) under the Solution based Processing of Photovoltaic Modules (SoPPoM) program. AGC is acknowledged for providing the SLG/Mo substrates.

Supporting information available

Supporting information are available and contains: SEM study of the morphology of the printed precursor layers with and without binder; ESR spectra of CISe layers; C-AFM/KPFM analysis of the printed CISe samples; Further TEM-EDX analysis performed on the printed CISe samples. This information is available free of charge via the Internet at http://pubs.acs.org.

References

[1] Jackson, P.; Hariskos, D.; Wuerz, R.; Wischmann, W.; Powalla, M. Compositional Investigation of Potassium Doped Cu(In,Ga)Se_2 Solar Cells with Efficiencies up to 20.8%, *Phys. Status Solidi RRL* **2014**, *8*, 219-222.

[2] Press release, *Solar Frontier Sets Thin-Film PV World Record with 20.9% CIS Cell*, Tokyo, April 02, 2014.

[3] Media release, *A New World Record for Solar Cell Efficiency*, Duebendorf, St. Gall, Thun, January 17, 2013.

[4] Hibberd, C. J.; Chassaing, E.; Liu, W.; Mitzi, D. B.; Lincot, D; Tiwari, A. N. Non-Vacuum Methods for Formation of Cu(In,Ga)$(Se,S)_2$ Thin Film Photovoltaic Absorbers, *Prog. Photovolt: Res. Appl.* **2010**, *18*, 434–452.

[5] Lincot, D. *et al*., Chalcopyrite Thin Film Solar Cells by Electrodeposition, *Solar Energy* **2004**, *77,* 725–737.

[6] Kemell, M.; Ritala, M.; Leskela, M. Thin Film Deposition Methods for $Culnse_2$ Solar Cells. *Critical Reviews in Solid State and Materials Sciences* **2005**, *30,* 1–31.

[7] Meadows, H.; Bhatia, A.; Depredurand, V.; Guillot, J.; Regesch, D.; Malyeyev, A.; Colombara, D.; Scarpull, M; Siebentritt, S.; Dale, P. Single Second Laser Annealed $CuInSe_2$ Semiconductors from Electrodeposited Precursors as Absorber Layers for Solar Cells, *J. Phys. Chem. C* **2014**, *118*, 1451–1460.

[8] Basol, B.M. Low Cost Techniques for the Preparation of $Cu(In,Ga)(Se,S)_2$ Absorber Layers, *Thin Solid Films* **2000**, *361–362*, 514-519.

[9] Lim, Y. S.; Jeunghyun, J.; Kim, J. Y.; Ko, M. J.; Kim, H.; Kim, B.; Jeong, U.; Lee, D. K.; Binder-Free Cu–In Alloy Nanoparticles Precursor and their Phase Transformation to Chalcogenides for Solar Cell Applications, *J. Phys. Chem. C* **2013**, *117*, 11930–11940.

[10] Kapur, V.K.; Bansal, A.; Le, P.; Asensio, O.I. Non-Vacuum Processing of $Cu(In,Ga)Se_2$ Solar Cells on Rigid and Flexible Substrates using Nanoparticle Precursor Inks, *Thin Solid Films* **2003**, *431–432*, 53-57.

[11] Kind, C.; Feldmann, C.; Quintilla, A.; Ahlswede, E.; Citrate-capped $Cu_{11}In_9$ Nanoparticles and Its Use for Thin-film Manufacturing of CIS Solar Cells, *Chem. Mater.* **2011**, *23*, 5269–5274.

[12] Mitzi, D. B.; Kosbar, L. L.; Murray, C. E.; Copel, M.; Afzali, A. High-Mobility Ultrathin Semiconducting Films Prepared by Spin Coating, *Nature* **2004**, *428*, 299-303.

[13] Milliron, D. J.; Mitzi, D. B.; Copel, M.; Murray, C. E. Solution Processed Metal Chalcogenide Films for P-type Transistors, *Chem. Mater.* **2006**, *18*, 587-590.

[14] Mitzi, D.B. Solution Processing of Chalcogenide Semiconductors via Dimensional Reduction, *Adv. Mater.* **2009**, *21*, 3141–3158.

[15] Liu, W.; Mitzi, D. B.; Yuan, M.; Kellock, A. J.; Chey, S. J.; Gunawan, O. 12% Efficiency $CuIn(Se,S)_2$ Photovoltaic Device Prepared Using a Hydrazine Solution Process, *Chem. Mater.* **2009**, *22*, 1010-1014.

[16] Krunks, M.; Mikili, V.; Bijakina, O.; Rebane, H.; Mere, A.; Varema, T.; Mellikov, E. Composition and Structure of $CuInS_2$ Films Prepared by Spray Pyrolysis, *Thin Solid Films* **2000**, *361–362*, 61–64.

[17] Press release, *Nanosolar's Flexible Foil Technology Achieves 17.1% Aperture Efficiency in NREL Tests*, PV Tech, Oct. 06, 2011.

[18] Todorov, T. K.; Gunawan, O.; Gokmen, T.; Mitzi, D. B. Solution-processed $Cu(In,Ga)(S,Se)_2$ Absorber Yielding a 15.2% Efficient Solar Sell, *Prog. Photovolt: Res. Appl.* **2013**, *21*, 82–87.

[19] Eberspacher, C.; Fredric, C.; Pauls, K.; Serra, J. Thin-film CIS Alloy PV Materials Fabricated using Non-vacuum, Particles-based Techniques, *Thin Solid Films* **2001**, *387*, 18-22.

[20] Yuan, M.; Mitzi, D.; Liu, W.; Kellock, A.; Chey, S.; Deline, V. Optimization of CIGS-Based PV Device through Antimony Doping, *Chem. Mater.* **2010**, *22,* 285–287.

[21] Nomura, S.; Matsuo, Y.; Wada, T. Fabrication of (Cu,Ag)$InSe_2$ Thin Films by a Combination of Mechanochemical and Screen Printing/Sintering Processes, *Mater. Res. Soc. Symp. Proc.* **2007**, *1012*, Y03–15.

[22] Kaelin, M.; Rudmann, D.; Kurdesau, F.; Zogg, H.; Meyer, T.; Tiwari, A.N. Low-cost CIGS Solar Cells by Paste Coating and Selenization, *Thin Solid Films* **2005**, *480-481*, 486-490.

[23] Haug, V.; Quintilla, A.; Klugius, I.; Ahlswede, E. Influence of an Additional Carbon Layer at the Back Contact‑Absorber Interface in Cu(In,Ga)Se_2, *Thin Solid Films* **2011**, *519*, 7464–7467.

[24] Zaghi, A. et al, J. Effect Of Selenium Content of $CuInSe_x$ Alloy Nanopowder Precursors on Recrystallization of Printed $CuInSe_2$ Absorber Layers during Selenization Heat Treatment, *Thin Solid Films* **2014**, in press (DOI: 10.1016/j.tsf.2014.10.003).

[25] Zaghi, A.; Buffière, M.; Brammertz, G.; Batuk, M.; Lenaers, N.; Kniknie, B.; Hadermann, J.; Meuris, M.; Poortmans, J.; Vleugels, J. Mechanical Synthesis of High Purity Cu–In–Se Alloy Nanopowder as Precursor for Printed CISe Thin Film Solar Cells, *Advanced Powder Technology* **2013**, in press (DOI: 10.1016/j.apt.2014.03.003).

[26] Norsworthy, G.; Leidholm, C.R.; Halani, A.; Kapur, V.K.; Roe, R.; Basol, B.M.; Matson, R. CIS Film Growth by Metallic Ink Coating and Selenization - Processing Perspectives, *Solar En. Mat. Solar Cells* **2000**, *60*, 127-134.

[27] Zaghi, A.; Buffière, M.; Brammertz, G.; Lenaers, N.; Meuris, M.; Poortmans, J.; Vleugels, J. Selenization of Printed Cu-In-Se Alloy Nanopowder Layers for Fabrication of $CuInSe_2$ Thin Films Solar Cells, *Thin Solid Films* **2014**, in press (DOI: 10.1016/j.tsf.2014.10.038).

[28] Niki, S.; Contreras, M.; Repins, I.; Powalla, M.; Kushiya, K.; Ishizuka, S.;Matsubara, K. CIGS Absorbers and Processes, *Prog. Photovolt: Res. Appl.* **2010**, *18*, 453–466.

TOC GRAPHICS (3.6 cm × 8.9 cm)

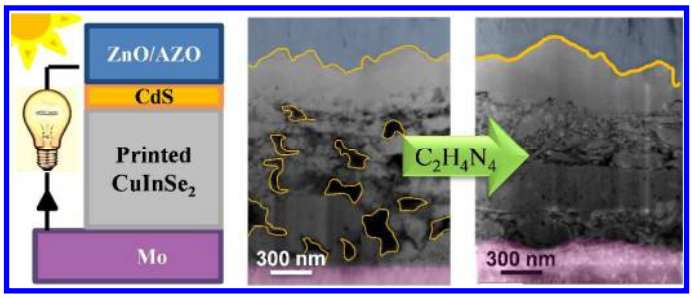

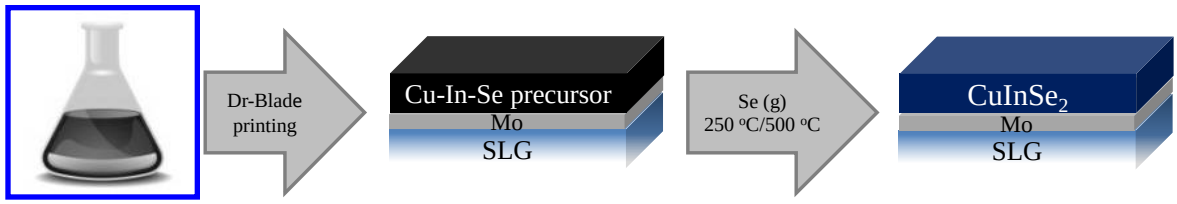

Cu-In-Se inks
0/10/20 wt.% DCDA

Precursor layers
a/b/c

CISe Samples
a/b/c

Figure 1. Scheme of the process used for the preparation of the samples studied in this work.

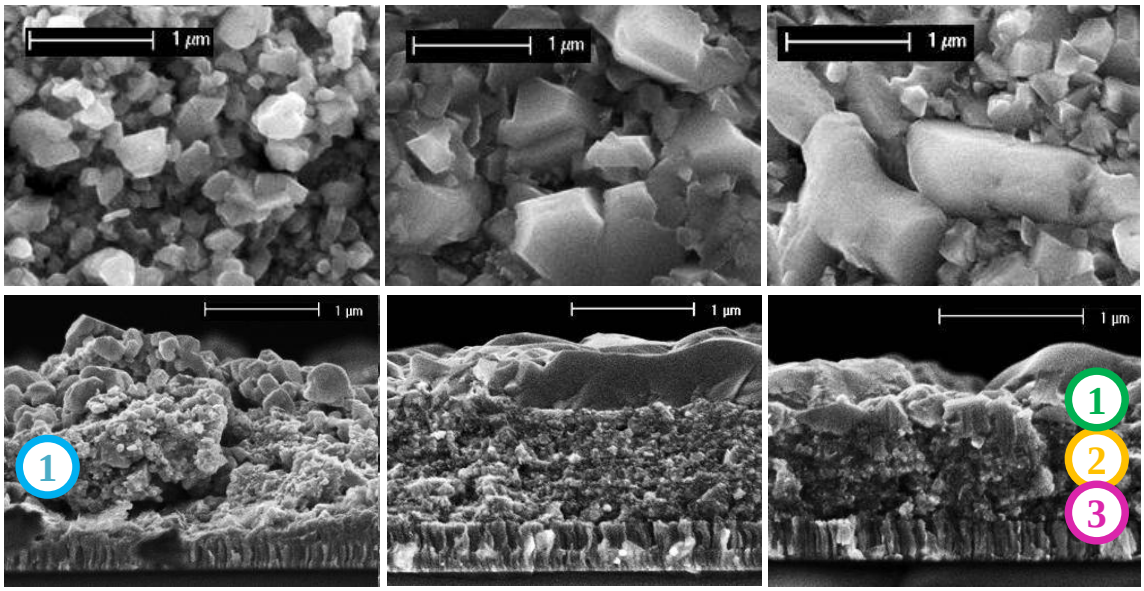

(a) 0 wt.% DCDA (b) 10 wt.% DCDA (c) 20 wt.% DCDA

Figure 2. Top view (upper row) and cross-section (lower row) SEM micrographs of printed CISe absorbers synthesized using (a) 0 wt.%, (b) 10 wt.% or (c) 20 wt.% of binder. The locations (1-3) indicates the in-depth positions of the XPS analysis (see figure 3).

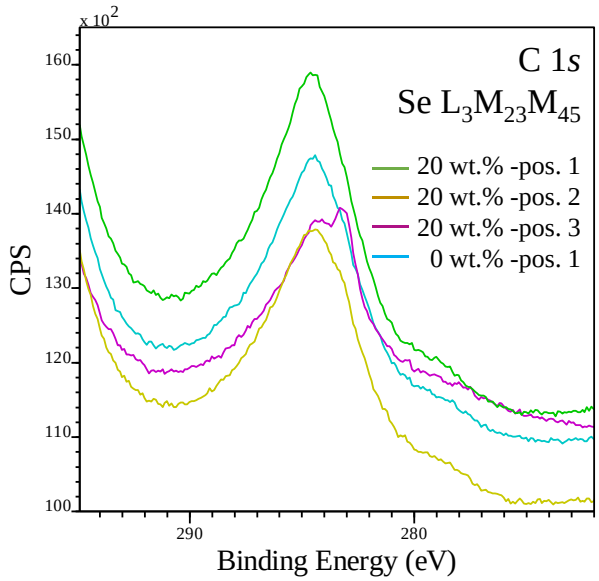

Figure 3. XPS spectra of the samples without and with 20 wt.% of DCDA in the region of the C 1*s* XPS peak. The in-depth position mentioned correspond to the locations indicated in figure 2.

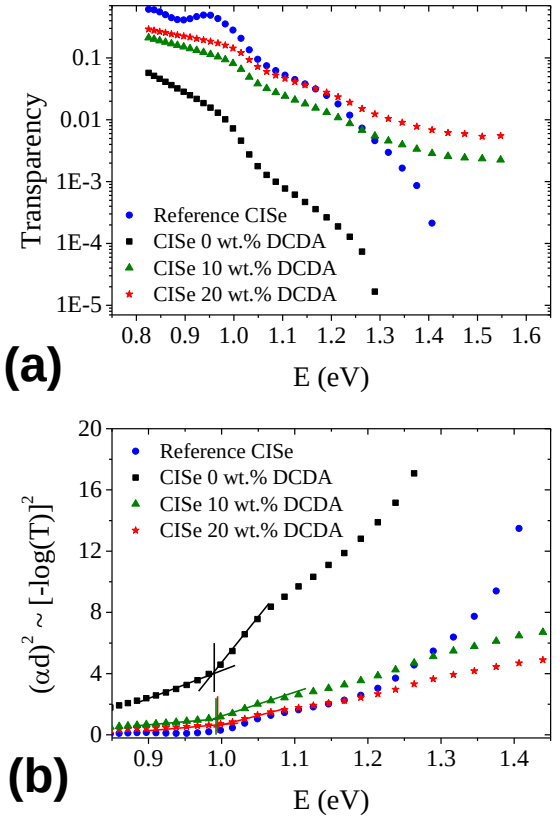

Figure 4. Optical (a) transparency (a) and relative absorption (b) spectra of the printed CISe samples without or with 10 wt.% or 20 wt.% of DCDA as compared to the co-evaporated CISe reference sample.

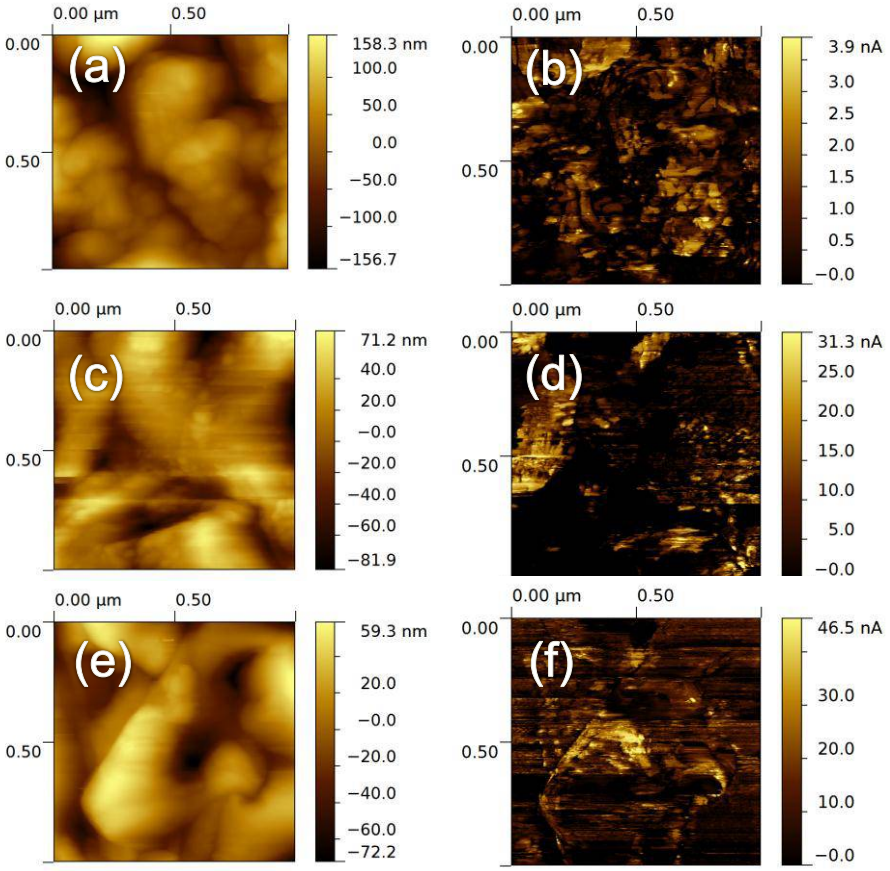

Figure 5. AFM (a, c, e) and C-AFM (b, d, f) mapping of the printed CISe thin films without (a, b), with 10 wt.% (c, d) or 20 wt.% (e, f) of DCDA binder.

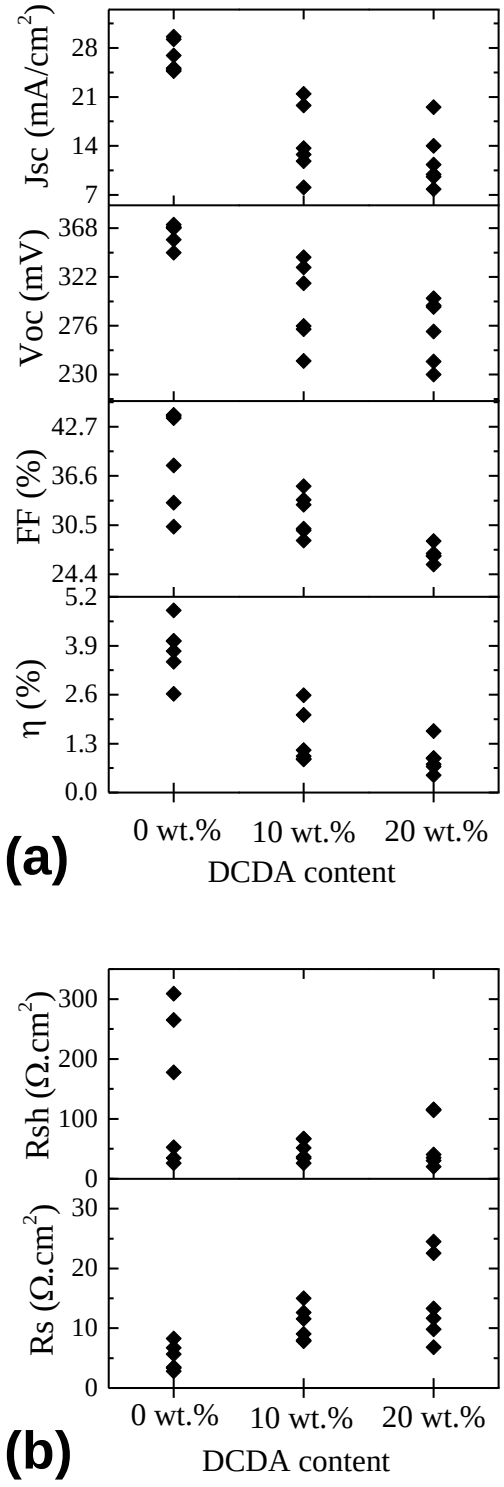

Figure 6. Electrical parameters ((a) V_{oc}, J_{sc}, FF, η and (b) R_s, R_{sh}) of the six best printed CISe solar cells using inks containing no binder, 10 wt.% or 20 wt.% of DCDA.

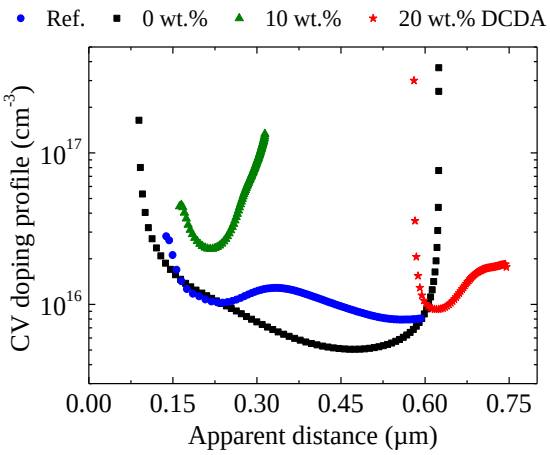

Figure 7. C-V doping profiles for the solar cells using printed CISe absorbers without binder, with 10 wt.% or 20 wt.% of binder and a co-evaporated CISe absorber as reference.

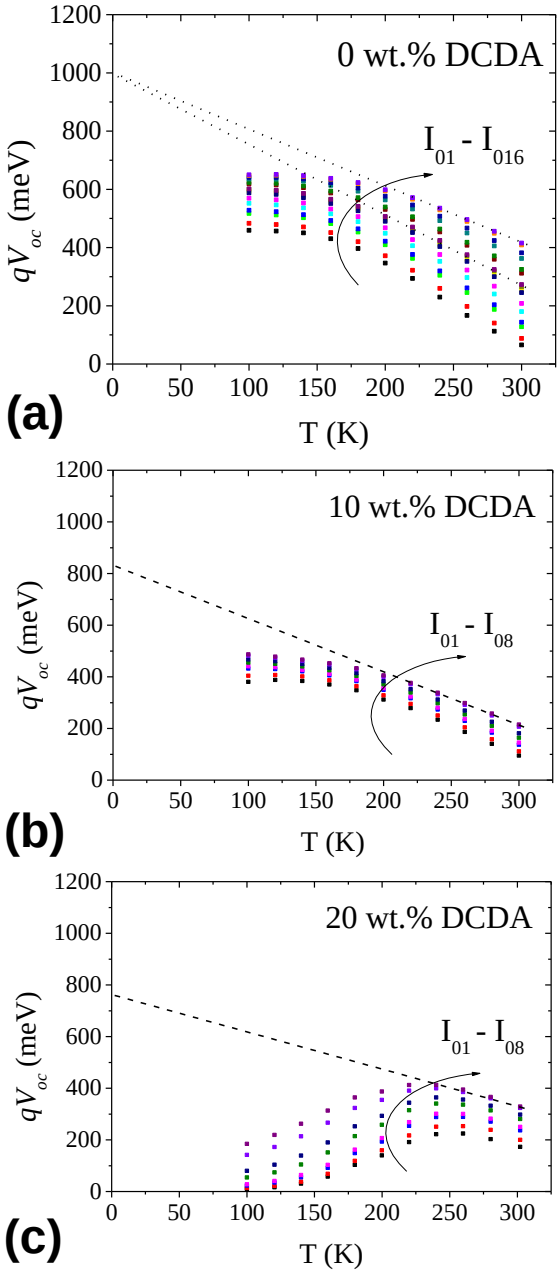

Figure 8. V_{oc} as function of temperature deduced from I-V-T measurements using different light intensities (from 0.1 sun to 1 sun) for the CISe devices (a) without and with (b) 10 wt.% or (c) 20 wt.% of binder.

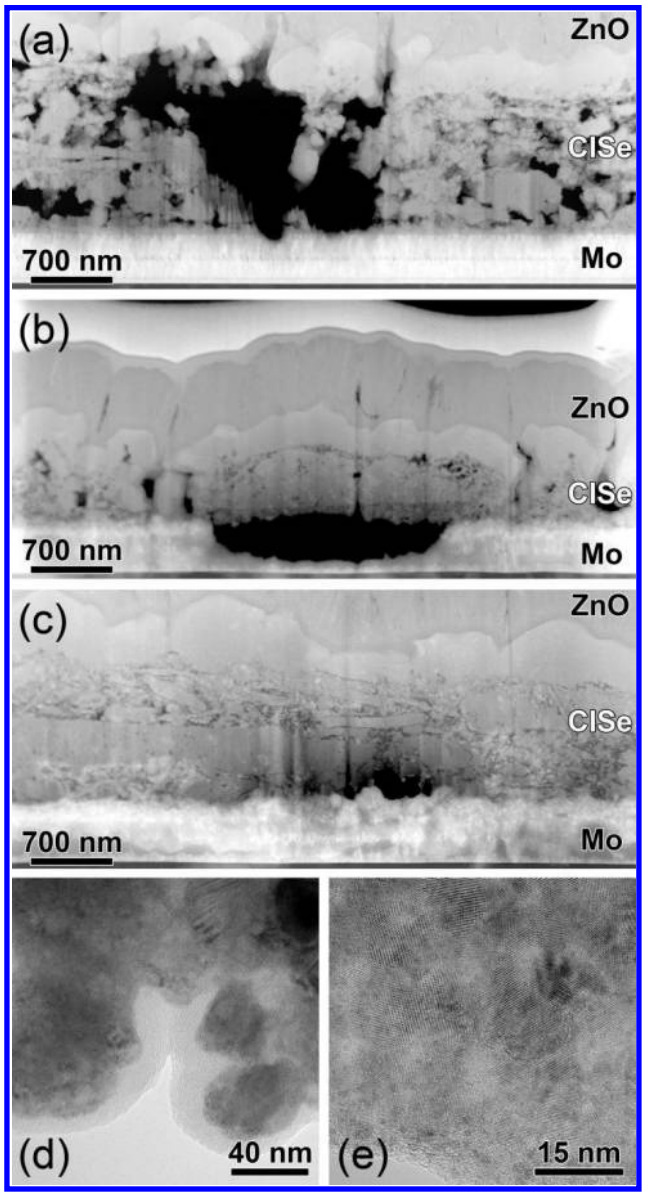

Figure 9. Cross-section STEM images of the best solar cells using CISe printed absorbers from an ink containing (a) no binder, (b) 10 wt.% or (c) 20 wt.% of DCDA. The TEM analysis of the free surface of the bottom CISe grains is shown in figure (d) (samples without binder) and (e) (sample with 20 wt.% of binder).

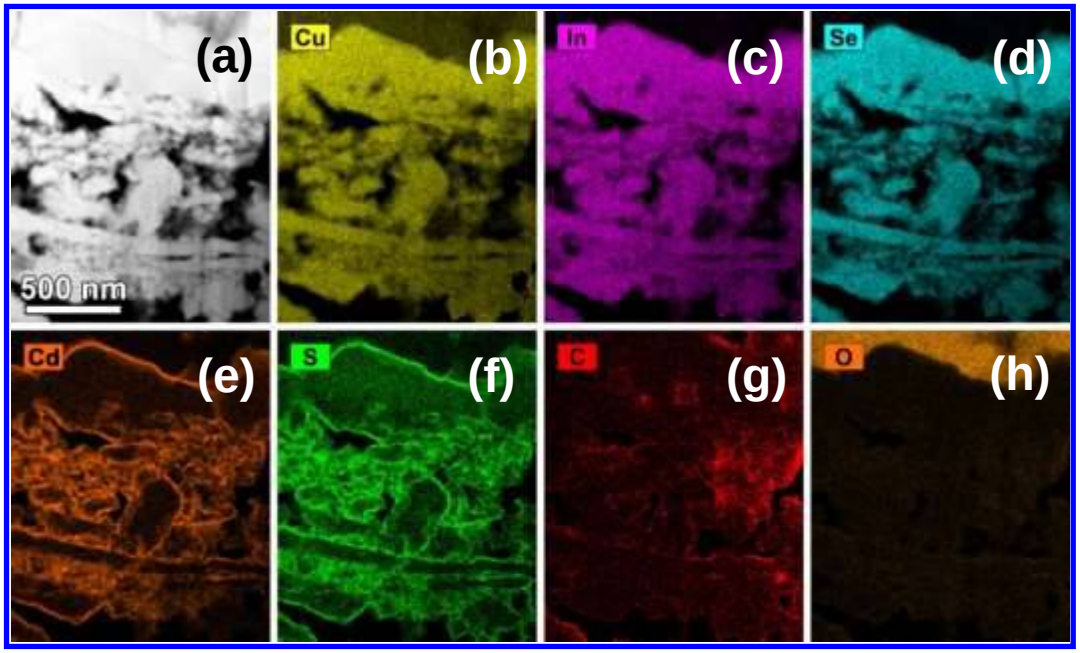

Figure 10. Cross-section HAADF-STEM image (a) and EDX maps of Cu (b), In (c), Se (d), Cd (e), S (f), C (g) and O (h) of the best printed CISe solar cell without binder.

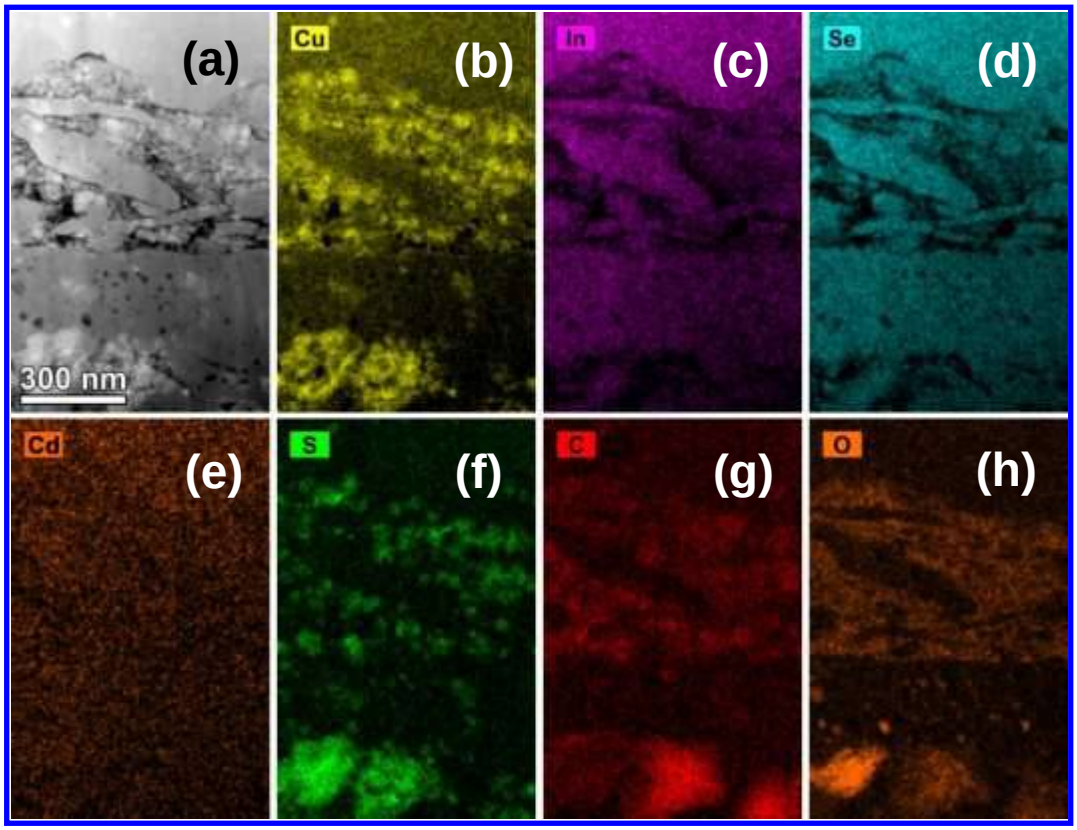

Figure 11. Cross-section HAADF-STEM image (a) and EDX maps of Cu (b), In (c), Se (d), Cd (e), S (f), C (g) and O (h) of the best printed CISe solar cell with 20 wt.% of binder.

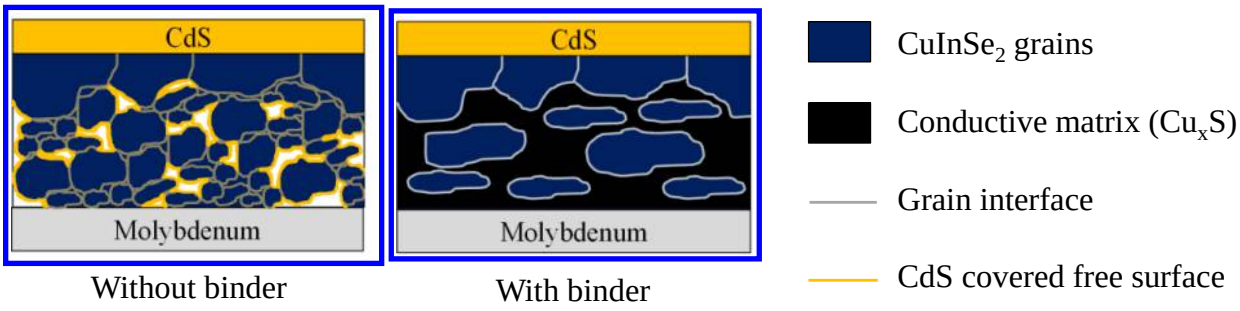

Figure 12. Model representing the morphology of CISe printed absorbers without and with binder.

Table 1. Chemical composition as measured by EDX and dangling bond densities related to C and Cu as determined from the ESR spectra of the printed CISe absorbers with different binder content values as compared to the co-evaporated CISe reference sample.

Sample	**Cu/In ratio**	**C density (g^{-1})**	**Cu^{2+} density (g^{-1})**
0 wt.% DCDA	0.87	3.0(±0.4)E+17	≤1.0E+13
10 wt.% DCDA	0.98	2.4(±0.4)E+17	≤1.0E+13
20 wt.% DCDA	0.94	2.5(±0.3)E+17	≤1.0E+13
$CuInSe_2$ ref.	0.90	≤1.0E+13	7.3(±0.9)E+17